The influence of deformation, annealing and recrystallisation on oxide nanofeatures in oxide dispersion strengthened steel

Karl Dawson, Gordon J. Tatlock
Centre for Materials and Structures, School of Engineering, University of Liverpool, UK

Abstract
This work demonstrates that Y-Ti oxide nanofeatures, observed in as-extruded, oxide dispersion strengthened steel, are structurally modified by cold forging. A 950 °C heat treatment promoted restructuring of the deformed particles and partial recrystallisation of the cold forged alloy. Transmission electron microscopy revealed that cuboid shaped nanofeatures were deformed during forging, which resulted in high number densities of lens shaped yttrium-titanium oxide particles. Annealing the forged alloy promoted partial recrystallisation of the ferritic matrix. Particle morphology reverted from lens shaped, as witnessed in the deformed material, to cuboid shaped oxide nanofeatures, identical to those observed in as-extruded material. Precipitation distributions evaluated in both recrystallised and recovering grains were indistinguishable from those first measured in the as-extruded alloy. TEM images revealed a widespread orientation relationship between the oxide precipitates and the recrystallised grains; registration with the ferrite lattice was omnipresent in both recovering and recrystallised grains.

1. Introduction

Ferritic oxide dispersion strengthened (ODS) steel, ODM401, once produced by Dour Metal s.r.o., is a nanostructured alloy and has a similar composition to MA957 ODS alloy formerly produced by the International Nickel Company (INCO) [1]. The microstructure of ODM 401 also displays similarities to MA957 material and both alloys, in their extruded condition, have very fine ferritic grains and high number densities (ca. 2×10^{23} m^{-3}) of 2 nm yttrium titanium oxide particles [2, 3].

ODS alloys are candidate materials for applications in future nuclear reactors, due to their good high temperature strength and apparent resistance to irradiation induced damage. These excellent properties can largely be attributed to the high number density of oxide nanofeatures which help strengthen the alloy at elevated temperatures but also act as sinks for transmutational He produced during irradiation. The entrapment of He at the particle matrix interface can mitigate some of the pernicious effects associated with He buildup at grain boundaries; which can lead to embrittlement.

A range of techniques has been used to demonstrate that precipitation of oxide nanofeatures can occur in ODS steels at temperatures between 650 °C and 850 °C [4-7]; however, Laurent-Brocq et al. [4] showed that precipitation is completed within the first 5 minutes of exposure to 800 °C. These findings indicate that oxide precipitation occurs in mechanically alloyed (MA) powders during the heating stage prior to consolidation by hot extrusion. Hence extrusion of MA ODS powders must involve interactions between the matrix and the high number density of nanofeatures that were already formed. Yet evidence of coherent nanofeatures, which display ubiquitous orientation relationships with the host matrix, has been presented in studies of extruded ODS alloys which contain yttrium and titanium [8, 9]. During hot extrusion, dynamic recrystallisation takes place and the matrix can recrystallise several times during

processing. Hence, in order to maintain the ORs which are observed, particles must continuously re-orient in registration with the new orientation of the recrystallizing grains.

This study uses cold forging and subsequent annealing to promote recrystallisation in ODM401 ODS alloy. The morphological transformations and chemistry of oxide nanofeatures was scrutinized to ascertain their behavior when influenced by deformation, annealing, recovery and recrystallisation.

2. Experimental procedure

Dour Metal's ODM401 alloy is a ferritic ODS steel produced by a powder metallurgical route; the composition of the steel is presented in table 1.

Table 1. Chemical composition (wt %) as measured by Hadraba et al. [1]

Cr	Ti	Mo	Y_2O_3	Fe	Al	C
13.6	0.85	0.29	0.25	Bal.	0.06	0.007

A cylindrical section of extruded ODM401 ODS alloy bar, approximately 9mm in length and 25 mm diameter, was cut into quadrants. A section of the material was retained for analysis in the as-extruded condition and a second section was annealed for 1 hour at 1300 °C. The remaining quadrant sections were cold forged (at room temperature) to a final length of approximately 4.5 mm, i.e. a compressive strain of $\varepsilon \approx 0.5$. A small section of the deformed material was retained for analysis and the remaining deformed material was annealed in laboratory air for 1 hour at 950 °C.

Thin foil specimens were prepared for transmission electron microscopy (TEM) by punching 3mm diameter discs from 0.5 mm thick sectioned alloy. The discs were then mechanically thinned to a thickness of less than 100 µm before being electropolished in a Struers Tenupol twin jet electropolishing system. An electrolyte of 5% perchloric acid in methanol, cooled to between -45 °C and -50 °C, produced electropolishing currents of approximately 0.06A when a potential of 30 volts was applied. Electropolished specimens were also used for electron backscattered diffraction (EBSD) experiments.

Electron microscopy and EBSD analyses were performed in an FEI Helios 600i dual beam focused ion beam (FIB) instrument fitted with an EDAX Digi-View system running OIM DC software. EBSD analysis was performed using a 20kV acceleration voltage, a 2.8nA beam current and step size of 80 nm.

Transmission electron microscopy (TEM) and chemical analysis was carried out using a JEOL 2100FC_S microscope, fitted with an EDAX windowless energy dispersive x-ray detector. The transmission electron microscope was operated at 200kV and analyses were made using both TEM and STEM modes.

Hardness measurements were recorded using a Matsuzawa Seiki micro-indentation hardness tester. A 1kg load was applied for 12 seconds; the mean values reported were taken from a minimum of 5 measurements.

3. Results

3.1 Microstructural changes to the matrix

The microstructure of as-extruded ODM401 ODS alloy exhibited ferritic grains elongated in the extrusion direction (Fig. 1a). A mean grain diameter of 0.4 µm (std. dev. ±0.3 µm) was determined from EBSD measurement of

transverse cross-sectioned specimens. Analysis of longitudinal cross-sectioned specimens showed that approximately 80% of the surface measured was occupied by grains with aspect ratios ≥ 5:1. A strong [110] fibre texture, parallel to the axis of extrusion, was also determined from the EBSD measurements.

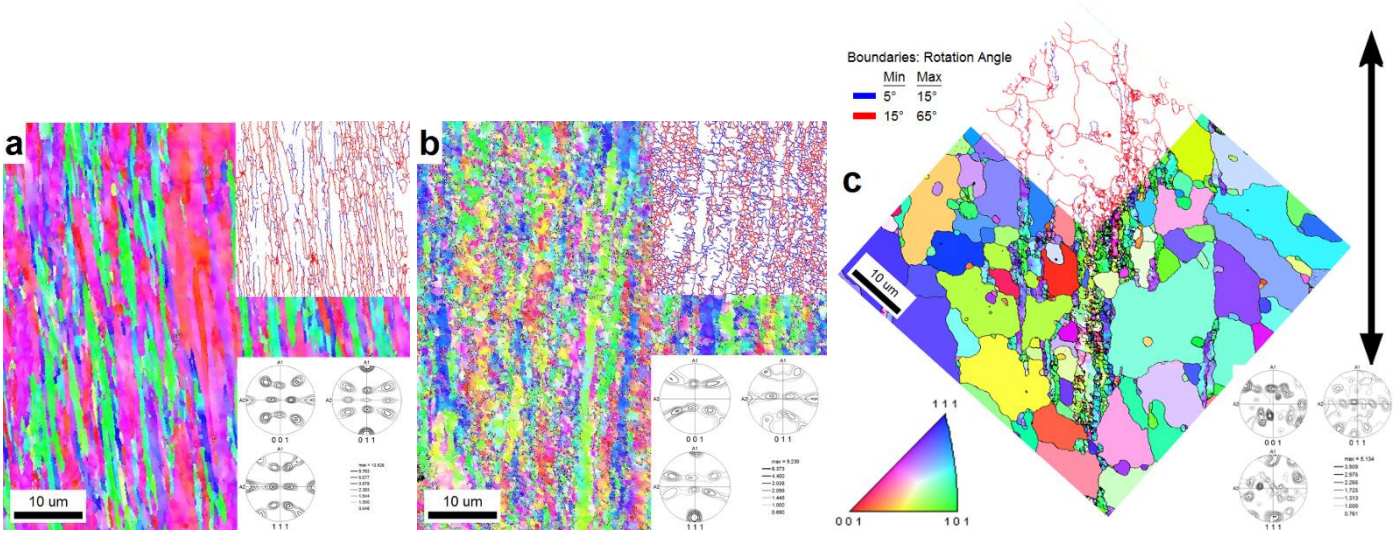

Fig. 1. EBSD Inverse Pole Figure (IPF) maps of (a) as-extruded, (b) as-deformed and (c) deformed and annealed alloy. Grain boundary maps are inset; medium angle (5 to 15°) and high angle (15 to 65°) grain boundaries are highlighted in blue and red respectively. Pole figure texture plots are also inset, in each case the direction *A1* corresponds, approximately, to the extrusion and compression axes, as does the double ended arrow.

Annealing for 1 hour at 1300 °C produced little change in alloy texture and grain size. A mean grain diameter of 0.5 µm (std. dev. = 0.4 µm) was measured from transverse x-sectioned specimens.

Sections of ODM401 alloy were cold forged, which resulted in a 50% reduction of length (approx.) parallel to the extrusion axis. SEM and EBSD analysis (Fig. 1b) were used to examine the microstructure of extruded material after deformation. The strong [110] fibre texture, which had been apparent in both the as-extruded and 1300 °C annealed specimens, was replaced by a [111] fibre texture. The size and aspect ratio of grains was reduced by the deformation process. The area fraction of grains with aspect ratios ≥ 5 was reduced from 80%, as observed in the as extruded alloy, to < 10% after cold forging. Kernal average misorientation (KAM) maps, calculated from EBSD data, indicated that local misorientations were greatly increased by cold forging; the ratio of low angle (2° to 5°) to high angle (15° to 180°) boundaries also increased.

Sections of as-deformed alloy were heat treated for 1 hour at 950 °C; this resulted in the widespread recrystallisation of the distorted matrix (Fig. 1c). In addition to the large (ca. 1 to 20 µm diameter) equiaxed recrystallised grains, distorted fine grains arranged in bands aligned approximately parallel to the axis of extrusion/deformation were retained. EBSD analysis of the partially recovered fine grain regions revealed a [111] texture parallel to the extrusion axis; this was similar to the texture observed in the as-deformed alloy. Some near surface effects on the microstructure were observed, but at distances greater than 0.5mm from the surfaces, to which the compressive load had been applied, the area fraction of recrystallised material was greater than 80%. EBSD KAM maps revealed local misorientation levels in the fine grained regions were greater than those observed in the large recrystallised grains; the degree of local misorientation in recrystallised grains was negligible.

Thin foil specimens of as-extruded, as-deformed and deformed and annealed alloy were analysed in the TEM in order to determine the effect of deformation and subsequent annealing on matrices and precipitate distributions. All specimens were cross-sectioned parallel to the direction of extrusion.

In the as-extruded alloy, dislocation entanglements formed boundaries between subgrains, whereas the internal regions of subgrains were in a relatively advanced state of recovery (Fig. 2a). In contrast, the microstructure observed in the specimen of as-cold forged alloy contained a greater density of dislocations. Deformation resulted in the formation of dislocation cells which were often only one or two hundred nanometers in diameter (Fig. 2b). After annealing, the ferritic matrix displayed a duplex structure comprised of large recrystallised grains and recovering sub-grains bounded by dislocation entanglements (Fig. 2c).

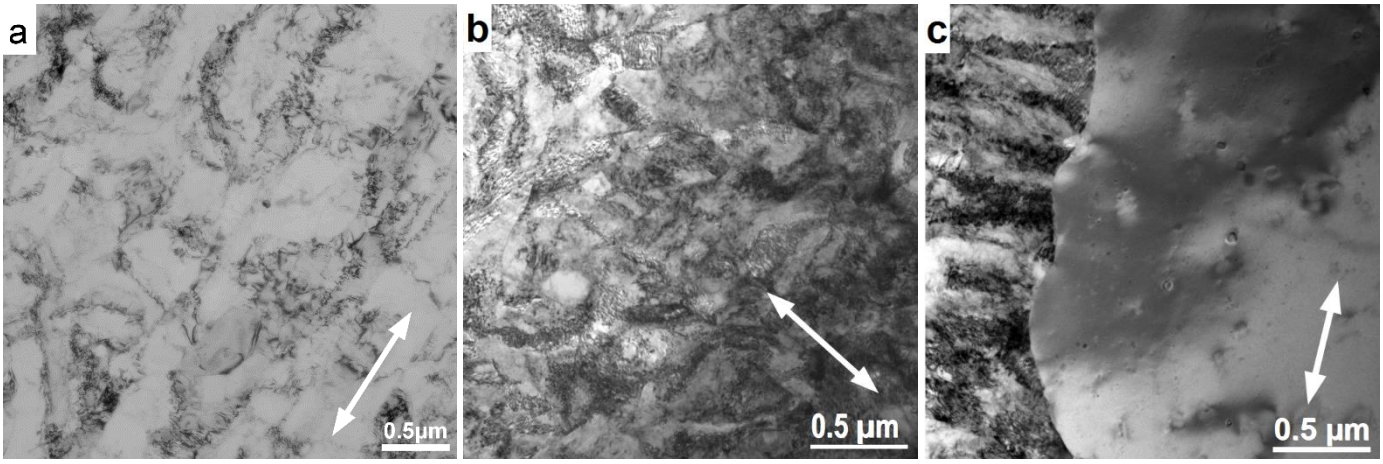

Fig. 2. TEM images showing (**a**) as-extruded alloy, (**b**) the as-deformed ferritic matrix and (**c**) recrystallised and recovering grains in the deformed and annealed material. (Arrows indicate the axes of both extrusion and deformation).

3.2 Analysis of Precipitates

TEM analysis of thin foil specimens, which had been sectioned from as extruded material, revealed a high number density (2×10^{23} m^{-3}) of 2 nm yttrium titanium oxide particles distributed homogeneously throughout the matrix. EDS measurements also revealed varied levels of aluminium in the nano-oxide particles. A ubiquitous cuboidal shape was displayed by the very small precipitates (Figs. 3a and 3b); previous work has identified similar precipitates as pyrochlore structured $Y_2Ti_2O_7$ oxides [2]. The nano-oxides displayed strong growth habits with facets parallel to the {011} and {200} ferrite planes. Both cube on cube and cube edge on cube (Baker-Nutting OR) orientation relationships between the oxide particles and matrix were reported.

After annealing extruded ODM401 alloy for one hour at 1300 °C the nano-oxides coarsened slightly to a mean diameter of approximately 5 nm. However, oxide-particle shapes, growth habits and orientation relationships remained identical to those observed in the as-extruded material.

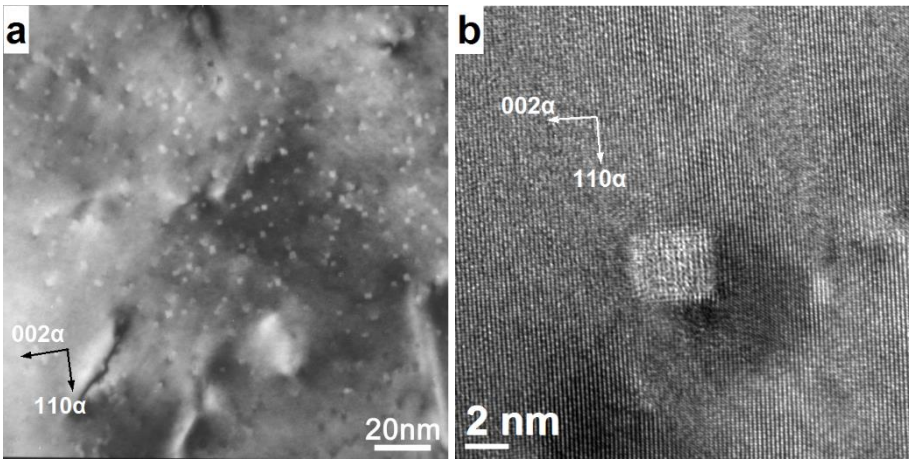

Fig. 3. TEM micrographs showing (**a**) a high number density of nano-oxides most of which (**b**) shared a common growth habit (as-extruded alloy).

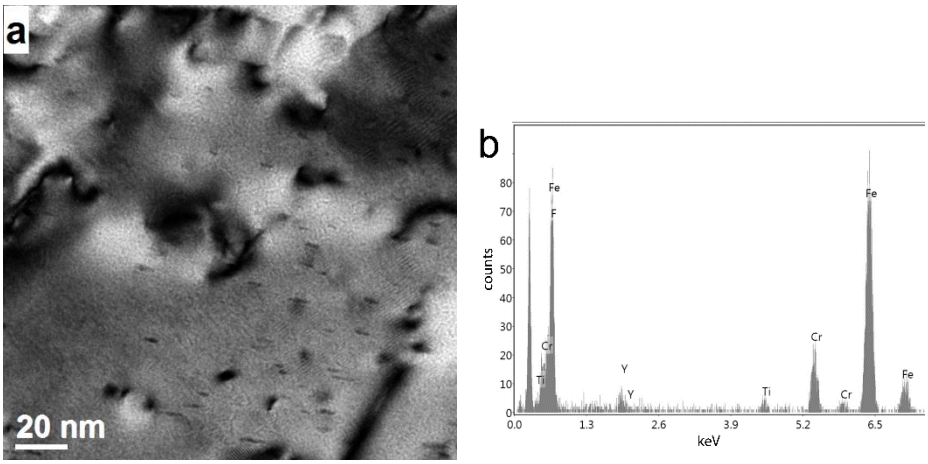

Fig. 4. (**a**) Filtered elastic EFTEM image showing lens shaped yttrium-titanium oxide particles with a common axis of elongation, in as-deformed alloy and (**b**) an EDS spectrum from a 5 nm lens shaped particle.

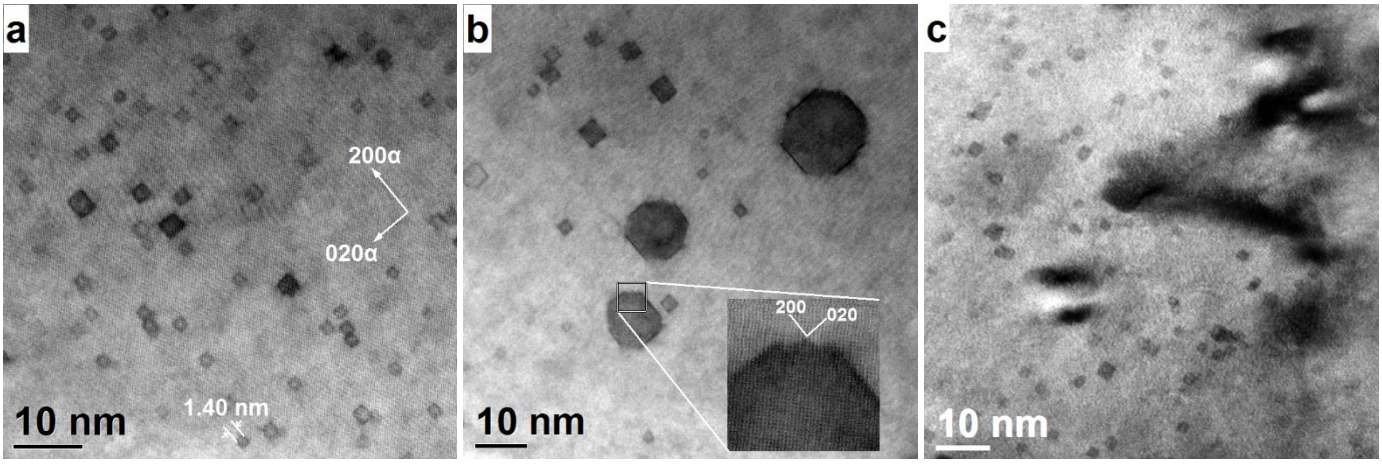

Fig. 5. BF-STEM images showing cube shaped nanofeatures in (**a**) a recrystallised grain, (**b**) particle faceting parallel to {200} planes and stepped {200} features forming {110} facets on larger particles (Figs. 5a and b show the same ferrite grain) and (**c**) (TEM) shows cuboid shaped particles in a recovering grain of deformed alloy annealed for 1 hour at 950 °C.

After cold forging, precipitates observed in the distorted matrix displayed an elliptical or lens like shape and cube shaped particles could no longer be detected. In general, the direction of elongation of the lens shaped particles, located in a single *grain or subgrain*, was uniform and unidirectional (Fig. 4a). Satisfactory imaging of particles in the deformed matrix was extremely difficult and slight variations in matrix orientation meant that good contrast was not always achieved, however, number density measurements indicated an approximate value of $N_V \approx 4 \times 10^{22}$ m^{-3} but this value might be subject to significant errors.

EDS analysis confirmed that the lens shaped particles, some as small as 5 × 2 nm (Fig. 4a), contained yttrium and titanium (Fig. 4b). Many more smaller particles, of a similar shape were also observed, but their composition could not be determined due to their diminutive size. In most cases, the structure of the particles could not be differentiated from that of the ferrite lattice; they appeared merely as high contrast features. However, some of the larger (c.a. 10 nm) lens shaped, Y-Ti enriched features shown in the images displayed periodicities, which differed from those of the matrix, but confirmed their crystallinity. The crystallinity, or lack of it, could not be confirmed in the smaller particles. In addition to the lens shaped oxides, larger spherical particles were also observed. Chemical measurements, using EDS, indicated that the largest spherical particles were titanium carbonitrides while some relatively small (10 to 20 nm) spherical Y-Ti oxides were also retained.

Sections of the cold forged ODS alloy were annealed for 1 hour at 950 °C and TEM thin foil specimens were produced; this enabled the analysis of oxide distributions in both recrystallised (Fig. 5 a and b) and partially recovered grains (Fig. 5c). Recrystallised grains contained high number densities ($N_V \approx 2 \times 10^{23}$ m^{-3} (±20%)) of nanofeatures within the size range 1 to 100 nm (Fig. 5a). The number density of larger (D > 5 nm) was insignificant when compared to the much greater number of 1 to 5 nm particles. Particle size distributions and their number densities (Fig. 6), were determined from TEM and STEM micrographs. Number densities were measured in as-extruded material and from recrystallised regions of the deformed and annealed specimens. Size distribution measurements were made in recovering fine grain areas of the annealed specimen but no number density data was recorded. However, the number densities in such regions did not appear to differ significantly from those in recrystallised grains, see figure 5, hence fine grain size distributions are included and plotted against the number densities determined in the recrystallised material (Fig. 6).

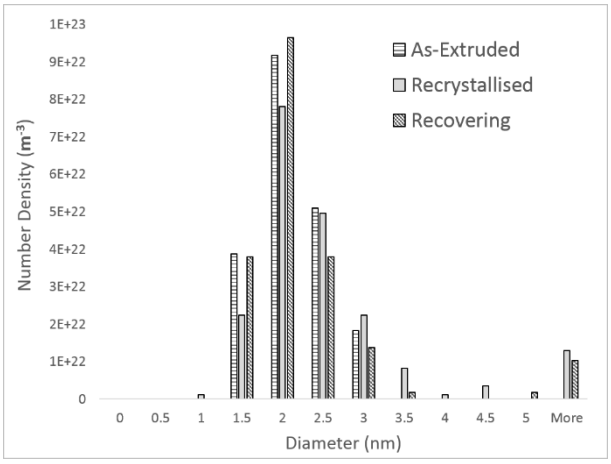

Fig. 6. Particle size distributions vs number density.

In general, the small Y-Ti oxides found in recrystallised grains were indistinguishable from those seen in recovering grains. These oxide nanofeatures exhibited a cuboid shape with distinct and well defined facets parallel to {002} ferrite planes (Figs. 5a, b and c). Many larger particles, observed in [001] oriented ferrite grains, appeared to display secondary faceting parallel to the {110} ferrite planes but on close examination it appeared that many of the {110} facets were actually composed of periodic ledges with edges parallel to the {200} planes (Fig. 5b). Hence, not only were particle morphologies and growth habits identical in recrystallised and recovering grains of annealed alloy but they were also indistinguishable from oxide nanofeatures first identified in the as extruded material.
The chemistry and crystal structures of oxide particles observed in the forged and annealed alloy were characterized using energy dispersive x-ray spectroscopy, atomic resolution TEM and scanning transmission electron microscopy (STEM). TEM images of the fine cube shaped particles failed to reveal any measurable difference between the crystal structures of the oxides and the ferrite matrix (Fig. 7a). There was also insufficient contrast in STEM images to enable differentiation between the crystal structures of the smallest oxides and the ferrite matrix; the smallest oxides appearing only as dark faceted features in a brighter matrix. The contrast measured in high angle annular dark field (HAADF) STEM images indicated that the oxide compounds had a lower atomic weight than the surrounding matrix. EDS analysis of the larger cuboid particles (c.a. 10 nm), confirmed the presence of yttrium and titanium.

Bright field (BF) STEM (Fig. 7b) and high angle annular dark field images (not shown) provided crystallographic information pertaining to larger precipitates. Yttrium titanium oxides displayed lattice spacings consistent with $Y_2Ti_2O_7$ (Fig. 7b). However, periodic variations in intensities, which should have been apparent in the atomic resolution z-contrast HAADF images, due to the alignment of atomic columns containing Ti, Y and mixed Y+Ti were not observed. A possible explanation for the lack of periodic intensity variations might be related to the crystal imperfections which were apparent in in many of the larger particles (Fig. 7b). Although the particles exhibit crystal structures that match $Y_2Ti_2O_7$, trace concentrations of aluminium were also detected in many of the particles. A possible explanation for the presence of aluminium is shown in figure 7b, where a low-z particle (determined from HAADF images) can be seen attached to the upper left corner of the 10 nm pyrochlore particle.

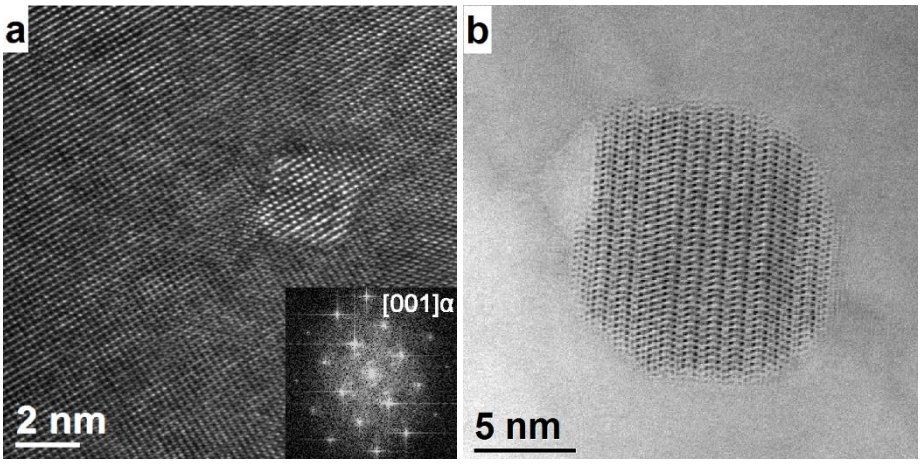

Fig. 7. (a) BF TEM image of a 2 nm cube shaped particle in a [001] oriented ferrite grain (FFT inset) and (b) BF STEM image of a particle displaying periodic intensities consistent with a [112] oriented Y2Ti2O7 pyrochlore crystal.

3.3 Hardness Measurements

Micro-indentation hardness measurements recorded from the as extruded and extruded alloy after annealing for 1 hour at 1300 °C were 367 HV1 and 281 HV1 respectively. Cold deformation of as-extruded alloy resulted in 10% increase in hardness to HV_{Def} = 405 HV1. Heat treatment and the corresponding changes in microstructure, i.e. partial recrystallisation, result in a drop in hardness (HV_{HT}) to approximately 315HV1.

4. Discussion

The hardness exhibited by the as-extruded alloy was reduced by approximately 23% during a 1 hour anneal at 1300 °C; although no recrystallisation or grain growth was observed. This suggests that the loss of hardness was influenced by changes in precipitate hardening, dislocation hardening and possibly some effects of solution strengthening. The small increase in hardness associated with cold forging, i.e. work hardening, saw an increase in hardness of only 10% but after heat treatment for 1 hour at 950 °C a reduction in hardness HV_{HT} = 315HV was measured. It was not surprising that annealing, in both cases, resulted in a loss of hardness. Nor was it unexpected that cold forging work hardened the alloy; this can be attributed to changes in dislocation density/configuration and changes to the grain/subgrain structure. By comparing the microstructures and hardness of the 1300 °C and 950 °C specimens, one might consider the importance of precipitation on room temperature properties. Quite clearly grain boundary hardening would be greatly reduced in the recrystallised regions; however, the size of indent (diagonals of approximately 77 µm using a 1kg load) meant that measurements always sampled a mixture of both recrystallised and small regions of recovering grains. It has been shown, in dual phase or duplex alloys, that hardness varies linearly with the volume fraction and individual properties of each phase, hence:

$$HV_{REX} = \frac{HV_{HT} - HV_{Def.}(1 - Vf_{REX})}{Vf_{REX}}$$

by weighting the overall hardness based on volume fractions of recrystallised (Vf_{REX} *=0.8*) and deformed ($Vf_{Def.}$) material, and the hardness of each component HV_{HT} = 315HV1 and $HV_{Def.}$ = 405HV1 respectively, it is possible calculate the hardness of the recrystallised grains as approximately 293HV.

Although this is based on the assumption that the hardness of deformed regions was not altered significantly by annealing and acceptance that the value might be subject to some variation. This indicated that recrystallised grains remained more resilient to plastic flow than the fine grain material in the 1300 °C annealed alloy. Hence, it appears that the effects of precipitation hardening are great and that just minor coarsening and reduced number densities, as measured in the 1300 °C annealed alloy, can have significant effect on the alloy's mechanical properties. This observation is supported by published results [10] which indicate that reductions in hardness correlate with oxide particle coarsening, and their reduced number densities, but at the same time, no discernable change in grain size or dislocation density was measured. Some caution is required however, as considerable changes in elemental distributions during aging, as were reported, might have influenced room temperature hardness.

The grain size distributions, grain aspect ratios and hardness of as-extruded ODM 401 alloy, measured during this study, were in keeping with values previously reported [1]. The present study also confirms that the microstructure of extruded ODM 401 can be considered comparable to that of ODS alloy MA957 [11]. The [110] fibre texture, which is characteristic of extruded BCC metals [12], has been observed previously in MA957 [13] and other ODS steels consolidated by extrusion [14-17].

The fine grained microstructure of ODM 401 showed excellent stability during short term exposure to high temperature; i.e. one hour at 1300 °C and negligible change in grain size was measured, by EBSD, between material in as-extruded condition and after annealing. Cunningham et al., [10] also reported on the remarkable microstructural stability displayed by MA957 during longer exposures but at more moderate temperatures. They measured no appreciable changes in grain size or dislocation density and only very minor coarsening of oxide particle distributions after a 19.5 thousand hour exposure at 1000 °C. It is suggested that high number densities of Y-Ti-O nanofeatures might influence the alloy's microstructural stability.

Secondary recrystallisation (abnormal grain growth) has been reported in MA957 alloy but only at temperatures greater than 1300°C. It has been demonstrated that microstructural instabilities, including grain growth, can be initiated at temperatures in region of 1330 °C [18] and complete recrystallisation occurs during heat treatments of 1 hour at 1450 °C [19]. This contrasts to the recrystallisation behavior of FeCrAl ODS alloys, such as ODM751, MA956 and PM2000, whose microstructures form massive grain structures due to secondary recrystallisation at lower temperatures. It is possible to generate significant volume fractions of secondary recrystallised PM2000 during 1 hour heat treatments at 1100 °C and complete recrystallisation, forming millimeter sized grains, can be achieved at temperatures as low as 1250 °C [20].

However, Regle [19], and Capdevila [18] revealed that the introduction of cold deformation could greatly influence the thermal stability of MA957 ODS alloy's microstructure and that recrystallisation temperatures were subsequently reduced from those ($T_R \geq 1330$ °C) found necessary to initiate recrystallisation in the as-extruded/as-received material. Similar observations have been made of FeCrAl ODS alloys, as reported by Zhang et al. [21] who annealed plastically deformed PM2000ODS alloy for 80 minutes at 715 °C promoting near complete recrystallisation; hence demonstrating that primary recrystallisation can be promoted, in different alloys, at temperatures much lower than those reported Regle and Capdevila.

More recently, the recrystallisation behavior of extruded and HIPed ODS alloy was compared by Dadé [22]. In their study, 14Cr YWT extruded alloy was cold forged to 40 and 70% reductions in thickness and subsequently annealed over a range of temperatures. In contrast to our findings for ODM401, their alloys underwent recovery only during annealing treatments at 950 °C and only 7% recrystallised fraction was realised after annealing the 40% deformed specimen at 1050 °C. In order to promote 80% recrystallisation, the alloy reduced by 40% had to be annealed at temperatures between 1250 °C and 1450 °C. The specimen reduced in thickness by 70% displayed 91% recrystallised fraction after annealing at 1150 °C. In contrast, a 1 hour anneal at 950 °C was sufficient to promote approximately 80% recrystallisation of ODM 401 alloy reduced in thickness by 50%. Hence it is evident that deformed ODM401 displays a lower resistance to recrystallisation even though the distributions of nano-oxides are similar in the two alloy systems.

Cold forged ODM401 alloy displayed a <111> fibre texture approximately parallel to the compression axis. This differs from the duplex <100> and <111> fibre texture reported in cold compressed PM2000 by Zhang [21]; however, the level of strain introduced by Zhang was far greater than studied here and the composition of PM2000 alloy is different to ODM 401. Duplex <111> and <100> compression textures are expected in BCC iron deformed at room temperature [23] but only when multiple slip planes are active, i.e. {110} + {112} or {110} + {112} + {123}. On occasions where only the {110} slip planes are active a {111} fibre texture is predicted [24]. It cannot be ruled out that the unique {111} fibre component detected in this work was related to the pre-existing extrusion texture, the operation

of only a single slip system or the different alloy composition. However, it is more likely that the lower levels of compressive plastic deformation introduced in this study produced a dominant [111] fibre texture, as this is the major compressive texture component in BCC metals [12] and the much weaker {100} fibre component was too weak for detection.

In the annealed material a {111} fibre texture was measured across the mixed recrystallised and recovering grains. This again, is in common with accounts in the literature, and although not detected, had a weak {100} fibre component existed in the as-deformed texture it would have been erased during recrystallisation [24, 25].

This study, and our previous work, has demonstrated that yttrium-titanium nanofeatures dominate particle distributions in as-extruded ODM401. It was also shown that precipitates exhibited ubiquitous cuboid and facetted cube morphologies. These very small particles displayed a uniform growth habit and faceting parallel to {002} and {011} ferrite planes. Although there remains some uncertainty regarding the crystal structure of Y-Ti-O nanofeatures, other studies have identified orientation relationships, morphologies and particle faceting, in a range of ODS alloys [3, 8, 9, 26], that are similar to those exhibited in ODM401. However, when present in extruded material, in which dynamic recrystallisation would lead to numerous matrix re-orientations, the oxide particles must have continually re-orientated to maintain a registry with the matrix. In general the nanofeatures and special orientation relationships appear to be the reserve of 12-14YWT type ODS alloys, where yttrium-titanium oxides dominate precipitate distributions. This said, recent research has shown that yttrium-aluminium nanofeatures, which display a common orientation in the matrix, can be formed in FeCrAl type ODS alloys [5, 27, 28]. However, these materials were all processed at relatively low temperatures, hence there is an indication that for orientation relationships to be retained, a critical temperature should not be exceeded.

After cold forging the cuboid shaped particles were no longer detected, instead, lens shaped particles, enriched in both yttrium and titanium were observed. In most cases particles in the same grain shared a common orientation of elongation, which most often, resulted in particle elongation perpendicular to the axis of compression.

It was evident from analysis of the annealed alloy that the yttrium titanium nanofeatures, which had changed shape from cuboid to lens shape during cold forging, underwent a second morphological transition during the heat treatment; since no lens shaped particles were observed in annealed material. Analysis of yttrium titanium nanofeatures in the annealed and partially recrystallised alloy showed that the distorted particles had been replaced by a particle dispersion dominated by yttrium-titanium nanofeatures with a cuboid shape. Not only were cuboid shaped particles observed, but they displayed uniform, ubiquitous orientation and faceting throughout entire recrystallised grains. It was evident that particles in recovering grains also adopted a cuboid shape and an identical orientation relationship with the ferrite matrix.

Particle re-structuring was apparent after annealing, which indicates that additional energy was required to activate the transformation mechanism. It is clear that, for these shape changes to occur, at least short range atomic movements were necessary. It is also evident that particles changed shape in both recovering and recrystallised grains, hence the passage of a recrystallisation front was not necessary for the restructuring of the nano-oxides. This later point indicates that dissolution and re-precipitation from a supersaturated matrix is not necessarily the mechanism by which particles restructure and re-orientate, however, neither does it rule out the dissolution/re-precipitation hypothesis.

In our previous work, which reported on the microstructural evolution of mechanically alloyed PM2000 FeCrAlY ODS powders during annealing, evidence was presented indicating dissolution and re-precipitation of precipitates, in

recrystallised alloy, which included a precipitate free zone adjacent to a recrystallizing interface. Naka et al. [29] also reported and showed clear evidence of dissolution and re-precipitation involving Y_2O_3 particles at recrystallizing interfaces but in a titanium based ODS alloy, again providing evidence of precipitate free zones. During the present study no precipitate free zones could be found but this might be expected if boundaries had remained static for any length of time.

A recent publication by Sallez [30] reports on precipitate interactions with grain boundaries during different stages of extrusion. Their findings support those reported previously by ourselves [5] and those reported by Naka [29]; they too observed oxide orientation changes adjacent to migrating boundaries similar to those presented here. Sallez also proposes a mechanism by which particles are dissolved at migrating boundaries and reprecipitated in their wake. Although this theory is in part consistent with our results it does not explain the restructuring of lens shaped particles in recovering grains and their apparent realignment with the matrix.

However, reports of particle re-structuring in ODS steel are not unique and Miller et al. [31] have recently demonstrated the ability of oxide nanofeatures to self-heal or re-precipitate after first being dissolved by ballistic interactions during ion irradiation studies. Further evidence of particle dissolution and re-precipitation is available in the findings of Wu et al. [3], who show widespread uniform growth habits of nanofeatures in the dynamically recrystallised grains of friction stir welded MA957 ODS material. This could only be possible if oxide particles had re-oriented en-masse and by chance arrived at a ubiquitous orientation, which is implausible. More realistic is the explanation that all particles were either re-structured and re-orientated, or dissolved at and re-precipitated behind recrystallizing interfaces. Interestingly, the growth habits and faceting appear identical to those reported in the present study and elsewhere in the literature [32]. Yu et al. [33], present one hypothesis, amongst others, that the coarsening of oxide particles in friction stir welded ODS steel could result from dissolution and re-precipitation events. They claim that if deformation levels introduced by friction stir welding were sufficient to break down oxides and drive their component atoms into solution, the heat and excess vacancies generated by the process would also enable their rapid re-precipitation. Their explanation appears feasible and fits with reports of coherent particles observed in friction stir welded ODS steel [34].

5. Conclusions

Plastic deformation, induced during cold forging, reduced the temperature required to recrystallise ODM401 alloy compared to those required to recrystallise the as extruded material. Annealing sections of the cold forged alloy, for 1 hour at 950 °C, promoted 80% volume fraction (approx.) of recrystallisation and produced a duplex grain structure comprised of large recrystallised and fine recovering grains.

The shape of Ti-Y oxide nanofeatures was modified by cold forging, from a ubiquitous cuboidal shape, observed in as extruded alloy, to elongated lens shaped particles. During heat treatment of the deformed alloy, sufficient energy was introduced to activate the restructuring of the lens shaped oxides.

In annealed alloy, both recovering and recrystallised grains contained high number densities of 2 nm, cube shaped, Y-Ti oxides. Nanofeatures observed in recrystallised grains and recovering grains displayed identical growth habits and orientation relationships with the ferrite matrix; these relationships were also identical to those observed in the as-extruded material. Particle size distributions and number densities were not affected significantly during the deformation and restructuring process and remained indistinguishable from those measured in the as-extruded

material. Furthermore, oxide particle size distributions and number densities measured in recrystallised grains could not be differentiated from those measured in recovering grains, hence other than atomic restructuring, precipitates appear to be unaffected by the passage of recrystallisation boundaries.

Our results demonstrate that it is possible to cold work, heat treat and recrystallise ODS material without negative effect on nano-oxide distributions; yet at the same time, manipulation of the ferritic grain structure can be achieved.

Acknowledgements

The authors wish to acknowledge the support and funding which was gratefully received from the Engineering and Physical Research Council (Grant No. EP/H018921/1). We are also grateful to Bohumil Kazimierzak, of Dour Metal s.r.o., for the provision of ODM401 alloy samples.

References

[1] H. Hadraba, B. Kazimierzak, L. Stratil, I. Dlouhy, J. Nucl. Mater. 417 (2011) 241-244. http://dx.doi.org/10.1016/j.jnucmat.2011.01.066

[2] K. Dawson, G.J. Tatlock, J. Nucl. Mater. 444 (2014) 252-260. http://dx.doi.org/10.1016/j.jnucmat.2013.10.003

[3] Y. Wu, E.M. Haney, N.J. Cunningham, G.R. Odette, Acta Mater. 60 (2012) 3456-3468. http://dx.doi.org/10.1016/j.actamat.2012.03.012

[4] M. Laurent-Brocq, F. Legendre, M.H. Mathon, A. Mascaro, S. Poissonnet, B. Radiguet, P. Pareige, M. Loyer, O. Leseigneur, Acta Mater. 60 (2012) 7150-7159. http://dx.doi.org/10.1016/j.actamat.2012.09.024

[5] K. Dawson, S.J. Haigh, G.J. Tatlock, A.R. Jones, J. Nucl. Mater. 464 (2015) 200-209. http://dx.doi.org/10.1016/j.jnucmat.2015.04.039

[6] C.A. Williams, P. Unifantowicz, N. Baluc, G.D.W. Smith, E.A. Marquis, Acta Mater. 61 (2013) 2219-2235. http://dx.doi.org/10.1016/j.actamat.2012.12.042

[7] M.J. Alinger, G.R. Odette, D.T. Hoelzer, J. Nucl. Mater. 329-333 (2004) 382-386. http://dx.doi.org/10.1016/j.jnucmat.2004.04.042

[8] J. Ribis, Y. de Carlan, Acta Mater. 60 (2012) 238-252. http://dx.doi.org/10.1016/j.actamat.2011.09.042

[9] J. Ciston, Y. Wu, G. Odette, P. Hosemann, Microsc. Microanal. 18 (2012) 760-761. http://dx.doi.org/10.1017/S143192761200565X

[10] N. Cunningham, Y. Wu, D. Klingensmith, G.R. Odette, Mater. Sci. Eng. A. 613 (2014) 296-305. http://dx.doi.org/10.1016/j.msea.2014.06.097

[11] P. Miao, G.R. Odette, T. Yamamoto, M.J. Alinger, D. Klingensmith, J. Nucl. Mater. 377 (2008) 59-64. http://dx.doi:10.1016/j.jnucmat.2008.02.042

[12] H. Hu, Texture, 1 (1974) 233-258. http://dx.doi:10.1155/TSM.1.233

[13] A. Alamo, H. Regle, J.L. Bechade, Advances in Powder Metallurgy, 1992, pp. 169-182.

[14] M.A. Montealegre, J.L. González-Carrasco, M.A. Morris-Muñoz, J. Chao, D.G. Morris, Intermetallics, 8 (2000) 439-446. http://dx.doi.org/10.1016/S0966-9795(99)00168-5

[15] M. Serrano, M. Hernández-Mayoral, A. García-Junceda, J. Nucl. Mater. 428 (2012) 103-109. http://dx.doi.org/10.1016/j.jnucmat.2011.08.016

[16] A. Steckmeyer, M. Praud, B. Fournier, J. Malaplate, J. Garnier, J.L. Béchade, I. Tournié, A. Tancray, A. Bougault, P. Bonnaillie, J. Nucl. Mater. 405 (2010) 95-100. http://dx.doi.org/10.1016/j.jnucmat.2010.07.027
[17] R. Kasada, S.G. Lee, J. Isselin, J.H. Lee, T. Omura, A. Kimura, T. Okuda, M. Inoue, S. Ukai, S. Ohnuki, T. Fujisawa, F. Abe, J. Nucl. Mater. 417 (2011) 180-184. http://dx.doi.org/10.1016/j.jnucmat.2010.12.069
[18] C. Capdevila, D.H.K.D.H. Bhadeshia, in: N. Hansen, X. Huang, D. Juul Jensen, E.M. Lauridsen, T. Leffers, W. Pantleon, T.J. Sabin, J. Wert (Eds.) Risø International Symposium on Material Science: Recrystallization - Fundemental Aspects and Relations to Deformation Microstructure, Risø, Denmark, (2000) 271-276
[19] H. Regle, A. Alamo, J. Phys. Paris. IV, 03 (1993) 727 - 730.
[20] C.L. Chen, G.J. Tatlock, A.R. Jones, Journal of Microscopy, 233 (2009) 474-481. http://dx.doi.org/10.1111/j.1365-2818.2009.03134.x
[21] Z.B. Zhang, N.R. Tao, O.V. Mishin, W. Pantleon, IOP Conference Series: Mater. Sci. Eng. 89 (2015) 012059.
[22] M. Dadé, J. Malaplate, J. Garnier, F. De Geuser, N. Lochet, A. Deschamps, J. Nucl. Mater. 472 (2016) 143-152. http://dx.doi.org/10.1016/j.jnucmat.2016.01.019
[23] L. Miyagi, M. Kunz, J. Knight, J. Nasiatka, M. Voltolini, H.-R. Wenk, J. Appl. Phys. 104 (2008) 103510. http://dx.doi.org/10.1063/1.3008035
[24] C.S. Barrett, Structure of Metals, 2nd ed., McGraw-Hill Publishing Company Ltd., London, 1952.
[25] I.L. Dillamore, W.T. Roberts, Metallurgical Reviews, 10 (1965) 271 - 380.
[26] A. Hirata, T. Fujita, Y.R. Wen, J.H. Schneibel, C.T. Liu, M.W. Chen, Nat Mater, 10 (2011) 922-926. http://dx.doi.org/10.1038/nmat3150
[27] P. Dou, A. Kimura, T. Okuda, M. Inoue, S. Ukai, S. Ohnuki, T. Fujisawa, F. Abe, Acta Mater. 59 (2011) 992-1002. http://dx.doi.org/10.1016/j.actamat.2010.10.026
[28] K. Dawson, A. Rao, G.J. Tatlock, A.R. Jones, IOP Conference Series: Materials Science and Engineering, 89 (2015) 012020.
[29] S. Naka, H. Octor, E. Bouchaud, T. Khan, Scripta Metall. Mater. 23 (1989) 501-505. http://dx.doi.org/10.1016/0036-9748(89)90440-7
[30] N. Sallez, C. Hatzoglou, F. Delabrouille, D. Sornin, L. Chaffron, M. Blat-Yrieix, B. Radiguet, P. Pareige, P. Donnadieu, Y. Bréchet, J. Nucl. Mater. 472 (2016) 118-126. http://dx.doi.org/10.1016/j.jnucmat.2016.01.021
[31] M.K. Miller, C.M. Parish, H. Bei, J. Nucl. Mater. 462 (2015) 422-427. http://dx.doi.org/10.1016/j.jnucmat.2014.12.048
[32] M.C. Brandes, L. Kovarik, M.K. Miller, M.J. Mills, J. Mater. Sci. 47 (2012) 3913-3923. http://dx.doi.org/10.1007/s10853-012-6249-x
[33] X. Yu, B. Mazumder, M.K. Miller, S.A. David, Z. Feng, Sci. Technol. Weld. Join. 20 (2015) 236-241. http://dx.doi.org/10.1179/1362171815Y.0000000002
[34] K. Dawson, S. Cater, G.J. Tatlock, C. Stanhope, Mater. Sci. Tech. 30 (2014) 1685-1690. http://dx.doi.org/10.1179/1743284714Y.0000000553